Published in final edited form as:
Nat Biotechnol. 2016 February ; 34(2): 175–183. doi:10.1038/nbt.3443.

Integration of electrophysiological recordings with single-cell RNA-seq data identifies novel neuronal subtypes

János Fuzik[#1,2], **Amit Zeisel**[#1], **Zoltán Máté**[4], **Daniela Calvigioni**[1,2], **Yuchio Yanagawa**[5], **Gábor Szabó**[4], **Sten Linnarsson**[1,6], and **Tibor Harkany**[1,2,6]

[1]Department of Medical Biochemistry and Biophysics, Karolinska Institutet, Stockholm, Sweden

[2]Department of Molecular Neurosciences, Center for Brain Research, Medical University of Vienna, Vienna, Austria

[4]Institute of Experimental Medicine, Hungarian Academy of Sciences, Budapest, Hungary

[5]Department of Genetic and Behavioral Neuroscience, Gunma University Graduate School of Medicine, Maebashi, Japan

[#] These authors contributed equally to this work.

Traditionally, neuroscientists have defined the identity of neurons by the cells' location, morphology, connectivity and excitability. However, the direct relationship between these parameters and molecular phenotypes establishing cellular heterogeneity has remained largely unexplored. Here, we present a method to obtain full transcriptome data from single neocortical pyramidal cells and interneurons after whole-cell patch-clamp recordings in mouse brain slices. In our approach, termed Patch-seq, a patch-clamp stimulus protocol is followed by aspirating the entire somatic compartment into the recording pipette, amplification by single-cell tagged reverse transcription in a tube reaction and Illumina sequencing. We show that Patch-seq reveals a close link between electrophysiological characteristics, responses to acute chemical challenges and RNA expression of neurotransmitter receptors and channels. Moreover, it distinguishes neuronal subpopulations that correspond to both well-established and, to our knowledge, hitherto undescribed neuronal subtypes. Our findings demonstrate the ability of Patch-seq to precisely map neuronal subtypes and predict their network contributions in the brain

Correspondence should be addressed to S.L. (sten.linnarsson@ki.se) or T.H. (tibor.harkany@ki.se or tibor.harkany@meduniwien.ac.at).
[6]S.L. and T.H. share senior authorship and correspondence.

Author contributions

J.F., A.Z., S.L. and T.H. wrote the paper. J.F. performed electrophysiology and the electrophysiology-based cell classification, and drafted figures. A.Z. performed single-cell RNA-seq and the transcriptome-based cell classification, and drafted figures. D.C. performed *post-hoc* morphological reconstruction of biocytin-filled neurons. Y.Y., Z.M. and G.S. provided unique reagents. S.L. and T.H. acquired funding and oversaw the research. All authors read and approved the manuscript for submission.

Accession code for RNA-seq data: GSE708744; http://www.ncbi.nlm.nih.gov/geo/query/acc.cgi?token=wxafweekthcrxqr&acc=GSE70844

Competing financial interests

The authors declare no competing financial interests.

Europe PMC Funders Author Manuscripts

The morphology, excitability, connectivity and neurotransmitter utilization of individual neurons underlie the distinct computations each neuronal circuit can perform in the nervous system[1-3]. Thus, the identification of distinct subclasses of neurons remains a key challenge in neuroscience. Neuronal taxonomy based on a combination of developmental, morphological and neurophysiological traits is well accepted, particularly for interneurons in the cerebral cortex[4-6]. These classification systems primarily rely on candidate marker analysis by a mixture of patch-clamp electrophysiology and single-cell semi-quantitative PCR (qPCR)[4,7-10]. More recently, advances in single-cell RNA sequencing (RNA-seq) in the central nervous system[11-13] led to the identification of novel cell-types. Particularly, RNA-seq allowed the molecular classification of neurons in the somatosensory cortex and CA1 subfield of the hippocampus into 47 subtypes, including 16 subclasses of interneurons[11]. Despite pioneering work using microarrays[14-16], multiplexed qPCR[17,18] and even proof-of-concept RNA-seq on single neurons[19], no robust method exists to simultaneously investigate the electrophysiology, morphology and transcriptome profiles of the same neuron. Combining patch-clamp electrophysiology and *post-hoc* morphological reconstructions with the resolution of quantitative RNA-seq in *single* neurons would present a potentially critical advance for neuronal classification as it can resolve transcriptome-wide variations in gene expression to reveal cell-type-specific determinants of neuronal cytoarchitecture and biophysical properties. Nevertheless, only Qiu *et al.*[19] attempted RNA-seq on material taken from three neurons through a patch pipette without prior patch-clamp recordings, which yielded RNA-seq data of variable quality.

Here, we describe *Patch-seq*, a method relying on sequencing RNA aspirated from the soma of single patch-clamp-recorded neurons. We validate *Patch-seq* transcriptomes by aligning them with larger single-cell datasets to achieve high-quality classification, particularly to resolve cortical (inter-)neuron types previously considered homogenous into distinct subtypes. We also show that *Patch-seq* is compatible with the *post-hoc* morphological analysis of neurons in optically cleared tissues, and produces a quantitative dataset that simultaneously resolves mRNAs for all known ion channels, receptors and synaptic proteins. Acute pharmacological probing of cortical interneurons established causality between RNA-seq-based predictions and experimentally observed neuronal responses *ex vivo*. Thus, *Patch-seq* is suited to discover molecular determinants of neuronal morphology and excitability.

Results

Data collection and characterization

We focused on cholecystokinin (CCK)-containing($^+$) GABAergic interneurons because their morphological and molecular features are thought to form a quasi-continuum from axon- to dendrite-targeting interneurons in cortical areas[3,5,11]. CCK$^+$ interneurons are the plastic and dynamic gate-keepers of neuronal circuits[20]. Their inactivation likely contributes to anxiety, mood disorders and schizophrenia[21,22]. As reliable histochemical detection of CCK$^+$ interneurons is particularly challenging, we established a dual-labeled CCK$^{BAC/dsRedT3}$::GAD67$^{gfp/+}$ mouse reporter[23,24] (Fig. 1a, Supplementary Fig. 1a), and sampled *dual* DsRed$^+$/GFP$^+$ interneurons in layers (L)1/2 of the somatosensory cortex. We took advantage of moderate CCK expression in cortical pyramidal cells[11] (DsRed$^+$ only) to

build a reference database of electrophysiological and molecular features that resolve cortical layer specificity for comparative analysis (Fig. 1a).

We first selected ~120 DsRed$^+$ cortical neurons in total for patch-clamp electrophysiology and morphological examination (as confirmed by epifluorescence microscopy prior to recording; Fig. 1a), of which 83 cells proved suitable for combined electrophysiology and RNA-seq analysis. Forty-five were interneurons (inhibitory types, "*I-types*"; Fig. 1b-f) and DsRed$^+$/GFP$^+$ with an additional 38 being pyramidal cells (excitatory types, "*Exc-types*"; Supplementary Fig. 1b-d). We only discarded neurons if their access resistance showed >20% deviation from baseline (Online Methods) or if their electrophysiology parameters did not resemble any *I-type* cluster (3 cells; *data not shown*). For each neuron, we recorded their location (cortical layer), and analyzed their passive and active membrane properties through a series of custom-written routines for whole-cell patch-clamp electrophysiology (on a HEKA EPC-10 controlled by PatchMaster 2.80; Supplementary Table 1). We also combined patch-clamp electrophysiology, biocytin filling, chromogenic (DAB) labeling and tissue clearing for the reconstruction of (axonal) morphology in optically cleared tissues[25,26] (Fig 1b-f). Our visualization method is also compatible with light-sheet[27] or two-photon microscopy in whole brain slices (300-350-μm thick), thus significantly reducing processing time and increasing the three-dimensional integrity of neuronal morphology.

Functional and morphological analysis of CCK interneurons

The most common nomenclature for (inter-)neurons[6] combines key biophysical and morphological features. Based on their pattern of postsynaptic target innervation, interneurons fall into one of three morphologically distinct subclasses: axo-axonic, perisomatic or dendrite-targeting cells[3,5-7,28]. Here, we first used patch-clamp electrophysiology to classify DsRed$^+$/GFP$^+$ interneurons in cortical L1 into 5 subclasses ("*I-types 1-5*, Fig. 1b-f, Supplementary Table 1 and Online Methods) purely based on their electrophysiological properties: *I-type 1* interneurons exhibited action potential (AP) accommodation with a low adaptation ratio. They began to spike at the onset of a rheobasic stimulus without producing a burst, demonstrated the smallest AP amplitude, the largest afterhyperpolarization (AHP) and most hyperpolarized resting membrane potential (V_{rest}, Fig. 1b). *I-type 2* cells had accommodating AP trains without producing burst firing. These cells displayed the highest AP amplitude, the steepest AP upstroke slope and the highest firing frequency of all recorded neurons. They did not demonstrate 'sag' depolarization indicating the activation of hyperpolarization-activated non-selective cationic currents (Fig. 1c). *I-type 3* interneurons produced AP bursts, shallowest AP upstroke and significant accommodation (Fig. 1d). Each AP burst consisted of 3-4 spikes after the first AP on 2-times threshold current. These neurons had a large afterdepolarization (ADP), as well as the largest 'sag' depolarization. *I-type 4* interneurons were accommodating cells that displayed a small ADP before a slow AHP; yet this was insufficient to produce a burst (Fig. 1e). These neurons had the highest input resistance amongst all interneuron subclasses examined. *I-type 5* interneurons exhibited irregular spiking, and fired APs without producing a burst (Fig. 1f). These cells had a small amplitude ADP on the falling trajectory of the AHP rise, and had the highest rheobase amongst the interneuron types assessed.

For comparison and validation, we examined the 38 pyramidal cells recorded in L2/3, L4 and L5 ("*Exc L2/3, L4 and L5*", Supplementary Fig. 1b-d, Supplementary Table 1 and Online Methods). L2/3 and L4 pyramidal cells (DsRed only) were categorized as non-bursting, accommodating and regular spiking (Supplementary Fig. 1b,c). In contrast, L5 pyramidal cells exhibited higher input resistance and pronounced ADP and a 2nd consecutive AP when stimulated at 2x the threshold current (Supplementary Fig. 1d).

Next, we used *post-hoc* morphological reconstructions to identify the axonal nests and dendritic arbors of the 5 putative interneuron subtypes (Fig. 1b-f). Our analysis revealed substantial differences in cell morphology, such as: *I-type 1* interneurons had equally-sized processes throughout, thus precluding their unequivocal assignment as axons or dendrites at the light-microscopy level. These processes concentrated in L1 and L2. *I-type 1* cells maintained gap junctions with neighboring non-pyramidal cells and even to L2/3 pyramidal cells, as shown by dye-loading experiments using Lucifer yellow (see also Fig. 6a,b). *I-type 2* interneurons had somatic diameters at least twice of *I-type 1* cells, and resided at the L1-L2 transition. Whereas their dendrites intruded into both L1 and L2, their axons were almost exclusively located in L2. *I-type 3* interneurons, similar to *I-type 1* cells, also had processes with homogenous diameters **yet** all were less than half of the process thickness of *I-type 1* cells. Their axonal arbor was less branched with the majority of processes coursing in L2. *I-type 4* cells had the majority of their elaborate axonal nests concentrated in L2 with some collaterals reaching as far as L4. Their dendrites targeted apically. *I-type 5* interneurons branched horizontally in L1 and upper L2. Rarely, we saw dye coupling between *I-type 5* interneurons and neighboring pyramidal cells, with less dense network labeling than for *I-type 1* cells**.** Cumulatively, the above correlated electrophysiology and morphological differences identify *I-type 1-5* CCK^{+} interneurons as *bona fide* interneuron subtypes. Their distinct features suggest a critical diversity of molecular determinants for cell identity, which can be interrogated by single-cell RNA-seq.

RNA sequencing of somatic aspirates

We next developed a method, called *Patch-seq*, for performing single-cell RNA sequencing on the same neurons that we characterized by patch-clamp electrophysiology. (Fig. 2, 3a-c and Online Methods). After testing the neurons in a series of current-clamp and voltage-clamp protocols within 20-25 min (*see above*), their entire somatic compartment was aspirated into the recording pipette. We found, using an iterative approach on ~140 cells (Supplementary Fig. 2), that applying a continuum of positive voltage pulses (to membrane potential +20 mV from holding potential −5 mV, each 5 ms in length with 5 ms intervals) reduced the loss of RNA by most efficiently holding negatively-charged RNA molecules in the pipette solution. Subsequently, the samples (0.8-0.9 μl) were ejected into lysis buffer (0.6 μl; Online Methods). RNA-seq was performed using a modified version of single-cell tagged reverse transcription (STRT-C1)[29,30] designed to handle low RNA input samples in a tube reaction (Online Methods).

Next, we subjected each sample to RNA-seq, generating 1.6 million raw reads per cell, of which 40% mapped uniquely to 2,068 distinct genes (on average, using UCSC conservative gene models, mainly protein-coding). On average, we observed 5,977 and 6,760 mRNA

molecules in excitatory and inhibitory neurons, respectively (Fig. 3d). This corresponds to an absolute capture efficiency of 7% per mRNA molecule per cell, as inferred by comparison with previously published single-cell data[11]. By comparison, RNA-seq of single neurons from the mouse neocortex can recover ~19,000 RNA molecules/neuron, mapped to ~5,000 distinct genes[11], with a capture efficiency of ~20%. We attribute losses to procedural differences, leakage during cell aspiration and/or binding of aspirated RNA to glass or plastic surfaces. Pan-neuronal markers[11] *Thy1* and *Stmn2* were detected in 79% and 87% of the cells, respectively.

To validate the quality of our RNA-seq data, we compared the results from inhibitory and excitatory neurons. As expected, *I-type* neurons expressed *Gad1* (the gene encoding GAD67; 41 of 45 cells) and *Gad2* (the gene encoding GAD65; 39 of 45 cells), as well as *Cck* (44 of 45 cells). Moreover, all subtypes of interneurons contained mRNAs for the vesicular inhibitory amino acid transporter (*Slc32a1*)[31] but lacked either vesicular glutamate transporter 1 (*Slc17a7*) or 2 (*Slc17a6*)[32,33]. Subsets of these interneurons also expressed mRNAs for neuropeptides (*Vip, Npy* and *Crh*) and Ca^{2+}-binding proteins (*Calb1*; Fig. 1g, 3e), markers known to co-exist with CCK in interneurons[5,6]. None of the cells (0/45) contained parvalbumin (*Pvalb*) mRNA transcripts. By contrast, *Exc-type* pyramidal cells only expressed *Slc17a7*, and to a lesser extent *Slc17a6*, but not *Slc32a1* (0 of 38 cells), along with considerably lower copy numbers of *Cck* mRNA (Fig. 3d). Thus, our RNA-seq data accurately reflect the major *functional* distinction between inhibitory and excitatory neurons in the cerebral cortex. Examining the RNA phenotypes of each of the 5 *I-types* amongst interneurons revealed a distinct pattern of common molecular markers (Fig. 1g, 3e). Thus, at this level of analysis, there was a one-to-one correspondence between transcriptionally- and electrophysiologically-defined cell identities.

Mapping neuronal identities on single-cell RNA-seq datasets

Electrophysiology is inherently limited in throughput. Consequently, the molecular classification of neurons from small and/or heterogeneous groups of cells is challenging because of the resulting low statistical power. To increase the reliability of our molecular classification, we took advantage of the single-cell dataset on somatosensory cortex we recently generated[11], containing >3,000 single-cell transcriptomes. We reasoned that if *Patch-seq* data could be aligned to this much larger dataset, we would be able to assign electrophysiological properties to molecularly better-defined neuronal subclasses. Even though this approach is not mandatory for neuronal classification, the increasing availability of reference datasets for major brain regions will enhance overall classification accuracy in small-sized sample populations.

We built a correlation-based classifier to assign each neuron from *Patch-seq* to one of the possible neuronal subtypes distinguished earlier[11]. The classifier used an iterative process of selecting relevant features (e.g., genes), ranking the candidate groups by correlation with any measured cell, and removing groups with lower correlation (Fig. 4a and Online Methods). None of the excitatory cells (0/38) were classified as interneurons, whereas a single interneuron (1/45) was classified as a L5 pyramidal cells (Fig. 4b).

The anatomical position, electrophysiology classification and molecular phenotype of pyramidal cells with high certainty corroborated their layer-specific L2/3-L5 identities (Fig. 4c). All of the measured interneurons were assigned to CCK^+ subclasses (Fig. 4d). None of the "*I-type*" interneuron subdivisions was classified into a single group molecularly. Instead, *I-types 1* and *5* were aligned to one set of closely related interneurons (Int11-Int14 in ref.[11]; Fig. 4d). Likewise, *I-types 2* and *3* were assigned to Int5-Int8, forming another subset of closely-related cell types. *I-type 4* showed exceptional heterogeneity with half of the cells assigned to each of these subsets. This shows that the combination of patch-clamp and RNA-seq methods benefits from an increased power of classification through the combination of real-life biophysical (and morphological) criteria and statistical predictions.

Molecular candidates to determine interneuron excitability

The depth of our molecular analysis allowed us to quantitatively assay the expression of channels, ion pumps and receptors in the *I-type* interneurons (Fig. 5a-c). Having our cells patch-clamp recorded, we could compare expression differences of any subunit detected with membrane potential changes (Fig. 5d). For example, Na^+/K^+ adenosine triphosphatase (ATPase) is a key electrogenic determinant of V_{rest} in excitable cells[34,35] . The quantitative expression of genes encoding ATPase subunits (*Atp1a1-Atp1b3*; Fig. 5a) closely and positively correlated with V_{rest} of each neuronal subtype in our dataset (for *Atp1a3* see Supplementary Fig. 3a).

Voltage-gated Cl^- channels, a family of poorly understood ion channels[36], are thought to modify V_{rest} by gating ion fluxes. Here, *Clcn3* was shown to positively correlate with V_{rest} (Supplementary Fig. 3b), potentially implicating these channels in determining subthreshold membrane potential fluctuations.

For AP frequency modulation, Kv3.1 (*Kcnc1*), a delayed rectifier K^+-channel, is broadly assumed to confer the capacity to discharge at high frequencies upon prolonged depolarization of fast-spiking interneurons[37]. Our data support this because interneurons firing in excess of pyramidal cells expressed ~3x higher RNA count/cell for *Kcnc1* ($p < 0.05$ for the whole *I-type* cell population). Similarly, coherence of the electrophysiology and RNA data was demonstrated by detecting cyclic nucleotide-regulated ion channel *Hcn1*. We saw no expression in "*I-type 1*" cells, where electrophysiology confirmed the lack of hyperpolarization-activated "sag" depolarization, a biophysical consequence of *Hcn1* activity (Fig. 1b; Supplementary Table 1). Thus, our RNA-seq data will allow predictions for future neurophysiology studies interrogating specific parameters of neuronal excitability.

Correlation matrix for use-dependent markers of neurons

Independent of any *a priori* classification, *Patch-seq* also permitted the analysis of correlations between gene expression and electrophysiological parameters. Many genes (748 out of 5,600) showed significant correlation with one or more electrophysiology parameters. We took advantage of our quantitative datasets, and asked if rendering mRNA copy numbers of ion channels and synapse-related proteins (167 passed our criteria, Online Methods) as predictors returns meaningful association with specific biophysical parameters of single APs or AP trains. We hypothesized that any sufficiently robust correlation (filtered for correlation

coefficients exceeding −0.4 and/or +0.4[11]; Supplementary Fig 4a,b) could be valuable for future studies if it allows for distinguishing any CCK$^+$ interneuron subtype. 24 genes (Clic4, Clip3, Cacna1g, Kcnma1, Kcnj11, Kcnc1, Apba2, Cacna1g, Cadps2, Exoc8, Gria1, Grin2b, Htr7, Kcnma1, Npy, Pak1, Pcdh8, Slc32a1, Slc6a17, Sort1, Stx4a, Syt6, Syt7, Tac2) had significant correlation with at least one parameter (Supplementary Fig. 4d-i). The main advantage of this approach is that it provides testable hypotheses by focusing on the preferential expression of genes in one but not another subset of interneurons. For example, synuclein-γ (*Sncg*), synaptotagmin 7 (*Syt7*), vesicle-associated membrane protein 4 (*Vamp4*) and the GABA synaptic reuptake transporter *Slc6a1* were grouped together and associated with AP parameters. Although the exact functional significance of these associations remains elusive, they provide candidates for the future molecular dissection of neuronal networks under physiological or pathological states.

Subtype-specific receptor repertoire in CCK interneurons—At any point in time, the intrinsic excitability of a neuron is dynamically tuned by its afferent inputs. An advantage of our *Patch-seq* dataset is that it contains information on most (if not all) ligand-gated ionotropic channels, metabotropic (G protein-coupled) and other receptors, which determine the net network load on each sampled neuron (Fig. 5a-c). This allows for inferences be made on the specificity and heterogeneity of afferent inputs.

For example, fast glutamatergic transmission relies on α-amino-3-hydroxy-5-methyl-4-isoxazolepropionic acid (AMPA) receptors expressed by all neurons. Its subunits, GluR1 (*Gria1*)-GluR4 (*Gria4*), are differentially expressed in various neuronal subtypes. As such, the fast kinetics of AMPA receptor inactivation and desensitization in interneurons is usually explained by their low levels of GluR2 (*Gria2*) subunit[38]. Here, we sampled 210 *Gria1* mRNAs in total in 45 interneurons (4.46 ± 5.3 mRNA molecule/cell) and 283 mRNAs cumulatively in 38 pyramidal cells (8.57 ± 8.08 mRNA molecule/cell; $p < 0.05$, mean difference of 3.61; Fig. 5b), thus quantitatively recapitulating earlier predictions by histochemistry and channel neurophysiology. Next, we examined the expression of the type 1 cannabinoid receptor (*Cnr1*) in our sample, which was reported to be highest in CCK$^+$ interneurons in the brain[39,40]. Here, we find that *I-type 1* cells lack appreciable *Cnr1* mRNA expression (12 *Cnr1* mRNA molecules in total), which contrasts with *I-type 2-5* subclasses (678 *Cnr1* mRNAs in total; Fig. 5c). These differences suggest another hitherto undescribed level of molecular complexity amongst cortical CCK$^+$ interneurons.

Many developmental biology studies utilize the serotonin (5-HT) receptor 3a (*Htr3a*) subtype to detect and classify CCK interneurons[4,41]. In our *Patch-seq* dataset, we observed no 5-HT3a expression in *I-type 1* cells (Fig. 6a,c), low *Htr3a* mRNA expression in *I-type 2* (*Calb*$^+$/*Npy*$^+$/*Vip*$^-$) cells and high mRNA copy numbers in *I-type 3* (*Vip*$^+$/*Npy*$^-$) and *I-type 4* (*Vip*$^+$/*Npy*$^+$, Fig. 6b,c) and *I-type 5* (*Vip*$^-$/*Npy*$^+$) interneurons. This suggests that *Htr3a* expression amongst CCK$^+$ interneurons might be more restricted than initially thought, likely leading to the under-sampling of CCK interneurons by *Htr3a*-driven genetic tags[41].

Subsequently, we expanded our analysis to all *Htr1a-Htr7* subtypes (Fig. 6c). None of the CCK$^+$ interneurons contained *Htr1a*, *Htr1b* or *Htr1d* mRNAs. Notably, *I-type 1* cells contained no mRNA copy for any of the 5-HT receptors. We validated our *Patch-seq* results

by measuring the excitatory effect of 5-HT on *I-type 1* ($n = 4$) *vs.* *I-type 4* ($n = 4$) interneurons (Fig. 6a,b) in whole-cell current-clamp experiments. While clamping the cells to 0 pA, 5 μM (*data not shown*) and 25 μM 5-HT (Fig. 6d,e *upper trace*) was bath-applied. Both subthreshold depolarization with 5 μM and suprathreshold depolarization with 25 μM 5-HT[42-44] was observed in both *I-type 1* and *4* interneurons. To dissect the origin of the depolarizing 5-HT effect and rule out indirect effects imposed by the neuronal network the recorded cell was embedded into, 10 μM 5-HT was microejected (”puffed”) onto interneuron somata. We controlled equal 5-HT load by coapplying a fluorescent tracer (Fig. 6d,e *middle*). Direct 5-HT application onto *I-type 1* interneurons did not cause depolarization (Fig. 6d, *bottom*). By contrast, *I-type 4* interneurons became readily depolarized (Fig. 6e, *bottom*). Our pharmacological rsults thus establish causality, considering that RNA-seq predicts 5-HT insensitivity in *I-type 1* interneurons due to the lack of any metabortopic or ionotropic 5-HT receptors. Moreover, the morphological reconstruction of the sampled interneurons (Fig 6a,b) is explanatory towards the depolarization of *I-type 1* cells upon bath application of 5-HT: *I-type 1* interneurons were dye-coupled to neighboring cortical non-pyramidal neurons, and even pyramidal cells. This allowed for interneurons to synchronize their membrane potentials through gap junctions[45], assigning *I-type 1* cells as ”passive followers” of network depolarization at suprathreshold 5-HT load. Thus, our *Patch-seq* data primed us to identify a CCK^+ interneuron with a 5-HT-driven effector behavior in its L1 microcircuit even if itself lacked 5-HT receptors. Overall, we suggest that our *Patch-seq* approach will help future systems (neuro-)biology investigations to rationalize diverse functional outcomes by providing a platform of identifying marks for specific modalities amongst neurons.

Discussion

The brain undoubtedly exhibits the highest level of cellular heterogeneity[10], and contains an large variety of neurons that differ in their morphology, connectivity, biophysical parameters and molecular phenotypes[5,6,46]. The taxonomy for neurons dates back to the first pioneers of neuroanatomy (e.g., Cajal and Golgi), who exclusively used morphological features, such as the size and topography of axonal and dendritic arbors, for classification and is now based on a wide array of neurophysiology, advanced histochemistry and RNA analyses[6]. Nevertheless, reliance on *known* candidate marks continued to dominate, and delayed the inception of unbiased classification. Moreover, the limited number of markers that could be probed at any given time (~20 for single-cell PCR and histochemistry)[7] together with the often mutually-exclusive experimental conditions that neurophysiology and single-cell molecular biology tools require limited detailed fingerprinting of cellular components in the brain.

We combined mouse genetics and patch-clamp electrophysiology to successfully target a distinct cohort of interneurons[5,47] in order to overcome existing limitations of classical function-structure analyses. In the CCK^+ cell population studied, we expected considerable neuronal diversity, which allowed us to improve and optimize *Patch-seq* to its present accuracy, even when low copy numbers of mRNA molecules were present. We first classified our CCK^+ interneuron sample from L1/L2 (but not from deep cortical layers[11] or hippocampal subfields[5,47]) into the 5 commonly identified subtypes. We further showed that

Patch-seq can identify a select number of molecular determinants that can be used to further subdivide CCK^+ interneuron subclasses. Each of these examples is significant because they reconcile previously reported sets of data on receptors (*5Ht3a*, *Cnr1*) and channels (*Hcn1*). We also note that *Patch-seq* can discover sets of cellular markers independent of other classification systems or *a priori* knowledge of the cell-type of interest. We also show that *Patch-seq* can help to form hypotheses e.g. about neurotransmitter-receptor relationships. We expect that similar approaches can be applied to essentially any neuronal subtype, and will help to avoid false-negative data (due to under-sampling of neuronal contingents) in cases when the resolution of available histochemical tools is limited or if suitable reagents are not available. As such, the lack of *Rgs12*, *Htr3a* and *Cnr1* mRNA transcripts in *I-type 1* interneurons raises the possibility that this abundant subclass might have been systematically missed in prior genetic reporter analyses, curtailing the analysis of their contribution to fundamental cortical network events.

The efficiency of mRNA capture in *Patch-seq* is lower than that in single-cell RNA-seq on dissociated tissues. However, it is still sufficient to efficiently sample even “low” expressed genes because of its extremely low rate of false-positive identification[11,12]. Thus, mRNA copy numbers even at the range of 1-5 molecules return meaningful associations. Moreover, the combination of *Patch-seq* with transgenic mouse technologies might allow the future exploitation of external (“spike-in”) reference standards (e.g. transgene products), thus facilitating positive cell identification. These methods together with the progressive decoding of regional heterogeneity in the nervous system through large-scale RNA-seq databases[11-13] can increase the stringency of neuronal classification. Such “reference atlases”, once available, will allow for precise hierarchical landscapes be built even when cell numbers from patch-clamp electrophysiology experiments are limited. However, *Patch-seq* can stand alone and give much more complete and accurate information about gene expression (~2,000 genes per cell) in selectively probed cell contingents, compared to previous methods (e.g. qPCR for 10-20 genes/cell)[6,7].

Patch-seq samples somatic material upon aspiration. For neurons, dendrites and axons occupy large spaces and their intracellular volume is considered significant. Therefore, one may argue that *Patch-seq* misses many mRNAs that are preferentially targeted to distant domains of axons or dendrites. Although some mRNA is actively transported into neurites[48], this does not mean that they are absent from the soma. On the contrary, most (if not all) mRNA species are more abundant in the soma than in neurites, and there is not a single known case of an mRNA that is localized exclusively outside the soma. This is true even for mRNAs thought to be actively transported into neurites, such as CamKIIα and spinophilin[49]. It is also known that the axon and dendrite contain much less total mRNA than the soma: axons are thought to contain about 1,000 – 4,500 mRNAs, whereas dendrites contain >2,500 mRNAs[49]. These numbers are at least an order of magnitude lower than the soma (which contains >100,000 mRNAs). As a result, sequencing the soma content can be expected to give a representative view of mRNA expressed by a neuron, although without information on which mRNAs are more or less efficiently transported into the neurites.

Another technical element that needs to be tightly controlled is the length of electrophysiology recordings because electrical stimuli might alter the transcriptome. Here,

we used 20-25 min protocols, which are compatible with the life-time of mRNA being on the order of many hours (median: 9 hours) with none being known as shorter than 1 hour[50]. The quickest transcriptional response known in any setting is the induction of immediate early genes (e.g., *c-Fos*, *Jun*, *Egr2*), and can be detectable after 30 min but peaks at 3 hours. However, removing immediate early genes did not affect cell-type identification. Thus, the impact of patch-clamp recordings that occur on a timescale less than one hour can be expected to have minimal impact on the RNA transcriptome.

In conclusion, *Patch-seq* can be expected to facilitate the characterization of transcriptome-wide changes in many experimental settings, thus contributing to a better understanding of fundamental physiological and pathological processes.

Online methods

Animals and husbandry

We generated a dual reporter mouse line (Supplementary Fig. 1a) by crossing parental lines that either expressed *Discosoma* red fluorescent protein (DsRed) under regulatory elements of the cholecystokinin (CCK) promoter on a bacterial artificial chromosome (BAC/CCK-DsRed)[24] or green fluorescent protein (GFP) knocked into the glutamate decarboxylase 67 gene ($GAD67^{+/gfp}$)[23]. The resulting $CCK^{BAC/DsRed}$::$GAD67^{+/gfp}$ line appeared anatomically normal, particularly without changes to brain size or deformities to its fine structures, including normal cell proliferation, migration (*data not shown*) and laminar distribution (Supplementary Fig. 1a). Animals were group-housed under 12:12 h/h light/dark cycle with *ad libitum* access to water and food. Animals of both sexes were used for neurophysiology experiments during postnatal days 17-23. Experiments on live animals conformed to the 86/609/EEC directive and were approved by the regional authorities on animal ethics (Stockholm Norra Djuretiska Nämnd; N512/12; Tierversuchsgesetz 2012, BGBI, Nr. 114/2012).

Preparation of brain slices, correlated differential-interference contrast and epifluorescence microscopy, superfusion

All experiments on interneurons were performed in L1/2 of the primary somatosensory cortex (S1). Coronal slices (300-μm thickness) were prepared on a VT1200S vibratome (Leica, Germany) in ice-cold artificial cerebrospinal fluid containing (in mM): 90 NaCl, 2.5 KCl, 1.25 Na_2HPO_4, 0.5 $CaCl_2$, 8 $MgSO_4$, 26 $NaHCO_3$, 20 D-glucose, 10 4-(2-hydroxyethyl)-1-piperazineethanesulfonic acid (HEPES), 3 Na-pyruvate, 5 Na-ascorbate (pH 7.4). Brain slices were then incubated at 22-24 °C for 60 min in a “recording” solution containing (in mM): 124 NaCl, 2.5 KCl, 1.25 Na_2HPO_4, 2 $CaCl_2$, 2 $MgSO_4$, 26 $NaHCO_3$, 10 D-glucose (pH 7.4). All constituents were from Sigma-Aldrich. Both solutions were aerated with carbogen (5% CO_2/95% O_2). Temperature was set to 33 °C (TC-10, Npi, Germany) in the recording chamber. Brain slices were superfused with “recording” solution at a rate of 4-6 ml/min.

Neurons were visualized by differential interference contrast microscopy on an Olympus BX51WI microscope. Next, the co-existence of DsRed and GFP in interneurons was

confirmed by epifluorescence microscopy using a mercury arc light source (USH-1030L, USHIO) and appropriate combinations of band- and long-pass excitation/emission filters (for GFP: U-MWIG3 [excitation: 460-495 nm; emission: 510-550 nm]; for DsRed: U-MWIBA3 [excitation: 530-550 nm; emission: >575 nm]).

Serotonin (5-HT; Tocris) was directly dissolved in the recording solution at final concentrations of 5 μM, 10 μM and 25 μM, and superfused at flow rates as above. Focal 5-HT ejection was performed using a microinjector (PDES-02TX-LA, Npi, Germany) after filling borosilicate glass capillaries (Hilgenberg, 3-4 MΩ) with 10 μM 5-HT. Pressure pulses of 500 mbar for 0.5 s were used with 30 s intervals. Pharmacological probing of the interneurons was carried out at 33°C.

Patch-clamp electrophysiology

Recordings were carried out with borosilicate glass electrodes (Hilgenberg, Germany) of 3-4 MΩ pulled on a P-1000 instrument (Sutter, USA). Electrodes were filled with an intracellular solution containing (in mM): 130 K-gluconate, 6 NaCl, 4 ATP-Na_2, 0.35 GTP-Na_2, 8 phosphocreatine-Na_2, 10 HEPES, 0.5 ethyleneglycolbis(2-aminoethylether)-*N,N,N′,N′*-tetraacetate (EGTA) and 0.5 mg/ml biocytin (pH 7.2 set with KOH). Whole-cell patch-clamp recordings were made on an EPC-10 triple amplifier (HEKA, Germany). Current clamp recordings were corrected for −9.99 ± 0.38 mV liquid junction potential between the intracellular and recording solutions, as measured against a 3M KCl-electrode. Resting membrane potential (V_{rest}, expressed as mVs) was measured in current-clamp mode at 0 pA current. Input resistance (R_m, expressed as MΩ) was calculated using linear regression established between electrotonic voltage responses (±15 mV from V_{rest}) and 500-ms current steps of increasing amplitude (10 pA increments). Membrane time constant (**τ**, ms) was averaged from 20 successive electrotonic voltage responses to hyperpolarizing (−40 pA) current steps and fitted with a single exponential. The “sag” depolarization, indicating the activation of hyperpolarization-activated non-selective cationic current (I_h) was calculated as the ratio of the peak negative voltage and steady-state negative voltage at a voltage response to hyperpolarizing current injections resulting in a steady-state voltage of −100 mV. AP threshold (AP_{thr}, mV) was defined as the voltage point where the upstroke’s slope trajectory first reached 10 mV/ms. AP amplitude was defined as the difference in membrane potential between AP_{thr} and AP at peak. AP rise time (ms) was the time from the AP_{thr} to the AP’s peak. AP duration (ms) was the time interval from AP_{thr} to the same voltage value during repolarization. The amplitude of afterhyperpolarization (AHP, mV) was defined as the difference between AP_{thr} and the most negative membrane potential attained during the AHP. AP decay time was calculated as the time from the AP’s peak to the peak of the AHP. Afterdepolarization (ADP) amplitude (mV) was defined as the difference between AHP peak and the most positive voltage value between AHP peak and the fast repolarization peak. In case of a lack of AHP, ADP was recognized as the most positive membrane potential between steady-state voltage and the peak of fast repolarization. Maximum AP up- and AP down-stroke were determined as the maximum and minimum of the geometrical differential of the AP (mV/ms), respectively. Maximum up- and down-stroke times were the times from AP_{thr} to reach maximum AP up- and down-stroke, respectively. These parameters were measured for *i*) the first AP elicited by 500-ms rheobasic current step; *ii*)

the first AP evoked along a 1-s current ramp of 0-150 pA and *iii*) the first three APs generated on a 750-ms trace as the voltage deflection of double of the rheobasic current was injected. Adaptation ratio was calculated as the ratio of the last inter-spike interval relative to the first five inter-spike intervals. Firing frequency (Hz) was determined at saturating current injections producing spike trains. AP amplitude accommodation was determined as a ratio of the average of the last three AP peaks relative to the first five AP peaks (difference defined in mVs). All parameters were measured (Supplementary Table 1) by applying manual procedures custom-written in Matlab (MathWorks, USA).

Tissue clearing and light microscopy

Brain slices containing biocytin-filled neurons were post-fixed in 4% paraformaldehyde in phosphate-buffer (PB, 0.1M, pH 7.8) at 4 °C overnight. Slices were repeatedly washed in PB and cleared using "CUBIC reagent 1" (25 wt% urea, 25 wt% *N,N,N',N'*-tetrakis(2-hydroxypropyl) ethylenediamine and 15 wt% polyethylene glycol mono-*p*-isooctylphenyl ether/Triton X-100) for 2 days[25,26]. After repeated washes in PB, biocytin localization was visualized using streptavidin-conjugated horseradish peroxidase (Vectastain Elite) using 3.3′-diaminobenzidine (DAB) as chromogen and H_2O_2 (0.05%) as substrate (in Tris-HCl, pH8.0). Slices were then re-washed in PB and submerged in "CUBIC reagent 2" (50 wt% sucrose, 25 wt% urea, 10 wt% 2,20,20'-nitrilotriethanol and 0.1% v/v% Triton X-100) for further clearing. *Post-hoc* neuroanatomy and neuronal reconstructions were performed using 40x and 60x objectives on a light microscope (Olympus BX51). Optionally, cleared tissues were imaged on a laser-scanning microscope (LSM780 and ZEN2013 software, Zeiss). Three-dimensional filaments of DAB-stained cells from 300 μm slices were reconstructed in Neurolucida (cx9000, Mbf Bioscience).

Cell harvesting for sequencing

A the end of each patch-clamp protocol, the micropipette was clamped to a holding potential (V_{hold}) of −5 mV. Prior to the harvesting procedure, a continuous series of depolarizing rectangular voltage pulses (5 ms at 5 ms intervals) were applied for 6-7 min with amplitudes of 25 mV from V_{hold}. The entire soma of each recorded neuron was aspirated into the micropipette slowly (~1-2 min) by applying mild negative pressure (−50 mPa). This procedure allowed us to retain a tight seal and to minimize RNA loss by keeping the RNA molecules in the pipette solution. When we broke contact, the recording pipette was pulled out from the recording chamber and then carefully rotated over an expelling 0.2 μl tube, where its content (0.8-0.9 μl) was ejected onto a 0.6-μl drop of lysis buffer pre-placed onto the side of a 0.2 ml tight-lock tube (TubeOne). The resultant sample (1.5 μl) was span down (20 s) at 24 °C to the bottom of the conical tube, stored at −80 °C and later subjected to in-tube reverse transcription (RT).

Lysis, cDNA synthesis and library preparation

Cell aspirates were dispensed into ~0.5 μl lysis mix consisting of 0.15% Triton X-100, 1 U/μl TaKaRa RNase inhibitor, 4 μM reverse transcription primer C1-P1-T31 5′-Bio-AATGATACGGCGACCACCGATCG TTTTTTTTTTTTTTTTTTTTTTTTTTTTTT-3′, 3.5 mM dNTP and 17.5 mM DTT. Samples were collected and stored at −80 °C until batch processing. Before reverse transcription, samples were thawed and lysed at 72 °C for 3 min,

then cooled to 4 °C. Immediately following the lysis step, 2 µl RT mix (1x SuperScript II First-Strand Buffer; Life Technologies) supplemented with 10.6 mM $MgCl_2$, 3.6 µM template-switching oligo C1-P1-RNA-TSO 5′-Bio-AAUGAUACGGCGACCACCGAUNNNNNNGGG-3′, 1.5 U/µl TaKaRa RNase inhibitor (Clontech), 1.45 M betaine and 21 U/µl Superscript II reverse transcriptase (Life Technologies)) were added and incubated at 42 °C for 90 min followed by 72 °C for 10 min. Following reverse transcription, 8 µl PCR mix (1x KAPA HiFi 2x ready mix and 240 nM C1-P1-PCR2 5′-Bio-GAATGATACGGCGACCACCGAT-3′) were added and PCR-amplified using thermal cycling as follows: 95 °C for 3 min (5 cycles), 98 °C 20 s, 62 °C 4 min, 72 °C 6 min, (9 cycles) 98 °C 20 s, 68 °C 30 s, 72 °C 6 min, (7 cycles) 98 °C, 30 s, 68 °C 30 s, 72 °C 7 min. Subsequently, PCR samples were cleaned using AMPure-XP beads (1:1 ratio; Beckman Coulter) and quantified by qubit (Life Technologies) on an Agilent bioanalyzer. Library preparation was done using tagmentation as described[29].

Illumina sequencing

Libraries were sequenced on an Illumina Hiseq2000 instrument using C1-P1-PCR2 as read1 (50 nt) primer and C1-TN5-U PHO-CTGTCTCTTATACACATCTGACGC as index read (8 nt) primer.

Data analysis

Read processing and molecule counts were performed as reported recently[11]. We only analyzed cells with >1,500 mRNA molecules/cell (excluding mitochondrial, repeat and rRNA) and if a complete catalogue of patch-clamp read-outs was available.

Alignment of interneurons and pyramidal cells on a cortical template

We used our recently described cortical dataset[11] to resolve each of the interneurons and pyramidal cells into one of template groups (from >3,000 dissociated cells). First, we narrowed down our search to one of the layer-specific pyramidal cell cohorts (S1PyrL1-L6) or interneuron groups (Int1-16), 22 groups in total. Because of a significant difference in the number of mRNA molecules detected, we designed our classifier on correlation measures rather than Euclidian distance. As feature selection is an important parameter for classification (e.g., which genes are “in use”), the classifier continuously updated the features for the groups compared. First, the median expression for every group (in the cortex dataset) was calculated. Because the standard deviation of the genes’ median expression (along groups) did not depend strongly on their mean expression, we selected genes (features) using a fixed threshold of standard deviation being >1.5 over the groups compared. The process was as follows: *i*) selection of a *Patch-seq* cell for classification; *ii*) setting the list of candidate groups to contain all 47 neuronal groups of the somatosensory cortex; *iii*) selection of genes for the current iteration, $std_{(\text{gene median expression})} > 1.5$; *iv*) calculation of the correlation between a *Patch-seq* cell and all candidate groups; *v*) ranking neuronal groups by their correlation to the *Patch-seq* cell (highest to lowest); *vi*) removal of those candidate groups that were <50% with their correlation; *vii*) if the list of candidate groups contained more than one group we looped back to step *iii*. If only a single candidate group was left, the *Patch-seq* cell was assigned to that particular group.

Correlation of gene expression and electrophysiology parameters

This analysis was aimed to identify mRNAs that might be predictors for electrophysiology parameters. We focused on mRNAs coding for ion channels, receptors and synaptic transmission-related proteins as sets of genes whose biological interpretation might be tested experimentally. We tested the correlation between all genes (5,600) that passed our baseline criteria (that is, more than 5 cells with non-zero expression, ~12% of data points) against all electrophysiology parameters (110). Along with the correlation, *p*-values for the null hypothesis of independent variables were calculated (permutation *p*-value shows similar results). For each gene separately, we used a false recovery rate (FDR) of 10% to declare a significant correlation. This was performed separately for every gene because otherwise the *p*-values strongly correlated and the assumptions for FDR were violated. Next, we focused only on ion channels, receptors and synapse-related genes (167 of these passed our above criteria). Correlation coefficients shown in Supplementary Fig. 4 are for genes that exhibited correlation (or anti-correlation) greater than 0.4.

Supplementary Material

Refer to Web version on PubMed Central for supplementary material.

Acknowledgements

We thank A. Juréus for DNA sequencing, and the CLICK Imaging Facility at Karolinska Institutet for making the Imaris software package available for neuronal reconstructions, T. Klausberger and E. Borók for discussions and assistance with Neurolucida reconstructions. Raw RNA-seq data were deposited with the Gene Expression Omnibus (www.ncbi.nlm.nih.gov/geo). This work was supported by the European Research Council (BRAINCELL 261063), the Swedish Research Council (to S.L. and T.H.); Human Frontier Science Program (to A.Z.), the European Commission 7th Framework Program (PAINCAGE, to T.H.), Hjärnfonden (to T.H.) and the NovoNordisk Foundation (to T.H.).

References

1. Fishell G, Hanashima C. Pyramidal neurons grow up and change their mind. Neuron. 2008; 57:333–338. [PubMed: 18255026]
2. Rakic P. Evolution of the neocortex: a perspective from developmental biology. Nat. Rev. Neurosci. 2009; 10:724–735. [PubMed: 19763105]
3. Klausberger T, Somogyi P. Neuronal diversity and temporal dynamics: the unity of hippocampal circuit operations. Science. 2008; 321:53–57. [PubMed: 18599766]
4. Tricoire L, et al. A blueprint for the spatiotemporal origins of mouse hippocampal interneuron diversity. J Neurosci. 2011; 31:10948–10970. [PubMed: 21795545]
5. Freund TF, Buzsaki G. Interneurons of the hippocampus. Hippocampus. 1996; 6:347–470. [PubMed: 8915675]
6. Ascoli GA, et al. Petilla terminology: nomenclature of features of GABAergic interneurons of the cerebral cortex. Nat. Rev. Neurosci. 2008; 9:557–568. [PubMed: 18568015]
7. Cauli B, et al. Molecular and physiological diversity of cortical nonpyramidal cells. J. Neurosci. 1997; 17:3894–3906. [PubMed: 9133407]
8. Cauli B, et al. Classification of fusiform neocortical interneurons based on unsupervised clustering. Proc. Natl. Acad. Sci. U. S. A. 2000; 97:6144–6149. [PubMed: 10823957]
9. Gupta A, Wang Y, Markram H. Organizing principles for a diversity of GABAergic interneurons and synapses in the neocortex. Science. 2000; 287:273–278. [PubMed: 10634775]
10. Markram H. The blue brain project. Nat. Rev. Neurosci. 2006; 7:153–160. [PubMed: 16429124]

11. Zeisel A, et al. Brain structure. Cell types in the mouse cortex and hippocampus revealed by single-cell RNA-seq. Science. 2015; 347:1138–1142. [PubMed: 25700174]
12. Romanov RA, et al. A secretagogin locus of the mammalian hypothalamus controls stress hormone release. EMBO J. 2015; 34:36–54. [PubMed: 25430741]
13. Usoskin D, et al. Unbiased classification of sensory neuron types by large-scale single-cell RNA sequencing. Nat. Neurosci. 2015; 18:145–153. [PubMed: 25420068]
14. Okaty BW, Sugino K, Nelson SB. Cell type-specific transcriptomics in the brain. J Neurosci. 2011; 31:6939–6943. [PubMed: 21562254]
15. Okaty BW, Sugino K, Nelson SB. A quantitative comparison of cell-type-specific microarray gene expression profiling methods in the mouse brain. PLoS. One. 2011; 6:e16493. [PubMed: 21304595]
16. Subkhankulova T, Yano K, Robinson HP, Livesey FJ. Grouping and classifying electrophysiologically-defined classes of neocortical neurons by single cell, whole-genome expression profiling. Front Mol. Neurosci. 2010; 3:10. [PubMed: 20428506]
17. Citri A, Pang ZP, Sudhof TC, Wernig M, Malenka RC. Comprehensive qPCR profiling of gene expression in single neuronal cells. Nat. Protoc. 2012; 7:118–127. [PubMed: 22193304]
18. Veys K, Labro AJ, De SE, Snyders DJ. Quantitative single-cell ion-channel gene expression profiling through an improved qRT-PCR technique combined with whole cell patch clamp. J Neurosci. Methods. 2012; 209:227–234. [PubMed: 22728251]
19. Qiu S, et al. Single-neuron RNA-Seq: technical feasibility and reproducibility. Front Genet. 2012; 3:124. [PubMed: 22934102]
20. Freund TF. Interneuron Diversity series: Rhythm and mood in perisomatic inhibition. Trends Neurosci. 2003; 26:489–495. [PubMed: 12948660]
21. Hashimoto T, et al. Alterations in GABA-related transcriptome in the dorsolateral prefrontal cortex of subjects with schizophrenia. Mol. Psychiatry. 2008; 13:147–161. [PubMed: 17471287]
22. Schmidt MJ, et al. Modulation of behavioral networks by selective interneuronal inactivation. Mol. Psychiatry. 2014; 19:580–587. [PubMed: 24322205]
23. Tamamaki N, et al. Green fluorescent protein expression and colocalization with calretinin, parvalbumin, and somatostatin in the GAD67-GFP knock-in mouse. J. Comp Neurol. 2003; 467:60–79. [PubMed: 14574680]
24. Mate Z, et al. Spatiotemporal expression pattern of DsRedT3/CCK gene construct during postnatal development of myenteric plexus in transgenic mice. Cell Tissue Res. 2013; 352:199–206. [PubMed: 23370601]
25. Tainaka K, et al. Whole-body imaging with single-cell resolution by tissue decolorization. Cell. 2014; 159:911–924. [PubMed: 25417165]
26. Susaki EA, et al. Whole-brain imaging with single-cell resolution using chemical cocktails and computational analysis. Cell. 2014; 157:726–739. [PubMed: 24746791]
27. Tomer R, Ye L, Hsueh B, Deisseroth K. Advanced CLARITY for rapid and high-resolution imaging of intact tissues. Nat. Protoc. 2014; 9:1682–1697. [PubMed: 24945384]
28. Kawaguchi Y, Kubota Y. Neurochemical features and synaptic connections of large physiologically-identified GABAergic cells in the rat frontal cortex. Neuroscience. 1998; 85:677–701. [PubMed: 9639265]
29. Islam S, et al. Highly multiplexed and strand-specific single-cell RNA 5' end sequencing. Nat. Protoc. 2012; 7:813–828. [PubMed: 22481528]
30. Islam S, et al. Quantitative single-cell RNA-seq with unique molecular identifiers. Nat. Methods. 2014; 11:163–166. [PubMed: 24363023]
31. Chaudhry FA, et al. The vesicular GABA transporter, VGAT, localizes to synaptic vesicles in sets of glycinergic as well as GABAergic neurons. J. Neurosci. 1998; 18:9733–9750. [PubMed: 9822734]
32. Fremeau RT Jr. et al. The expression of vesicular glutamate transporters defines two classes of excitatory synapse. Neuron. 2001; 31:247–260. [PubMed: 11502256]
33. Kaneko T, Fujiyama F, Hioki H. Immunohistochemical localization of candidates for vesicular glutamate transporters in the rat brain. J. Comp Neurol. 2002; 444:39–62. [PubMed: 11835181]

34. Kirischuk S, Parpura V, Verkhratsky A. Sodium dynamics: another key to astroglial excitability? Trends Neurosci. 2012; 35:497–506. [PubMed: 22633141]
35. Arganda S, Guantes R, de Polavieja GG. Sodium pumps adapt spike bursting to stimulus statistics. Nat. Neurosci. 2007; 10:1467–1473. [PubMed: 17906619]
36. Mindell JA, Maduke M. ClC chloride channels. Genome Biol. 2001; 2 REVIEWS3003.
37. Baranauskas G, Tkatch T, Nagata K, Yeh JZ, Surmeier DJ. Kv3.4 subunits enhance the repolarizing efficiency of Kv3.1 channels in fast-spiking neurons. Nat. Neurosci. 2003; 6:258–266. [PubMed: 12592408]
38. Angulo MC, Lambolez B, Audinat E, Hestrin S, Rossier J. Subunit composition, kinetic, and permeation properties of AMPA receptors in single neocortical nonpyramidal cells. J Neurosci. 1997; 17:6685–6696. [PubMed: 9254681]
39. Tsou K, Brown S, Sanudo-Pena MC, Mackie K, Walker JM. Immunohistochemical distribution of cannabinoid CB1 receptors in the rat central nervous system. Neuroscience. 1998; 83:393–411. [PubMed: 9460749]
40. Katona I, et al. Presynaptically located CB1 cannabinoid receptors regulate GABA release from axon terminals of specific hippocampal interneurons. J. Neurosci. 1999; 19:4544–4558. [PubMed: 10341254]
41. Munoz-Manchado AB, et al. Novel Striatal GABAergic Interneuron Populations Labeled in the 5HT3aEGFP Mouse. Cereb. Cortex. 2014
42. Varga V, et al. Fast synaptic subcortical control of hippocampal circuits. Science. 2009; 326:449–453. [PubMed: 19833972]
43. Ferezou I, et al. HT3 receptors mediate serotonergic fast synaptic excitation of neocortical vasoactive intestinal peptide/cholecystokinin interneurons. J. Neurosci. 2002; 22:7389–7397. [PubMed: 12196560]
44. Caiati MD, Cherubini E. Fluoxetine impairs GABAergic signaling in hippocampal slices from neonatal rats. Front Cell Neurosci. 2013; 7:63. [PubMed: 23641199]
45. Tamas G, Buhl EH, Lorincz A, Somogyi P. Proximally targeted GABAergic synapses and gap junctions synchronize cortical interneurons. Nat. Neurosci. 2000; 3:366–371. [PubMed: 10725926]
46. Rakic P. A century of progress in corticoneurogenesis: from silver impregnation to genetic engineering. Cereb. Cortex. 2006; 16(Suppl 1):i3–17. [PubMed: 16766705]
47. Morozov YM, Freund TF. Postnatal development and migration of cholecystokinin-immunoreactive interneurons in rat hippocampus. Neuroscience. 2003; 120:923–939. [PubMed: 12927199]
48. Zivraj KH, et al. Subcellular profiling reveals distinct and developmentally regulated repertoire of growth cone mRNAs. J Neurosci. 2010; 30:15464–15478. [PubMed: 21084603]
49. Holt CE, Schuman EM. The central dogma decentralized: new perspectives on RNA function and local translation in neurons. Neuron. 2013; 80:648–657. [PubMed: 24183017]
50. Schwanhausser B, et al. Global quantification of mammalian gene expression control. Nature. 2011; 473:337–342. [PubMed: 21593866]

Europe PMC Funders Author Manuscripts

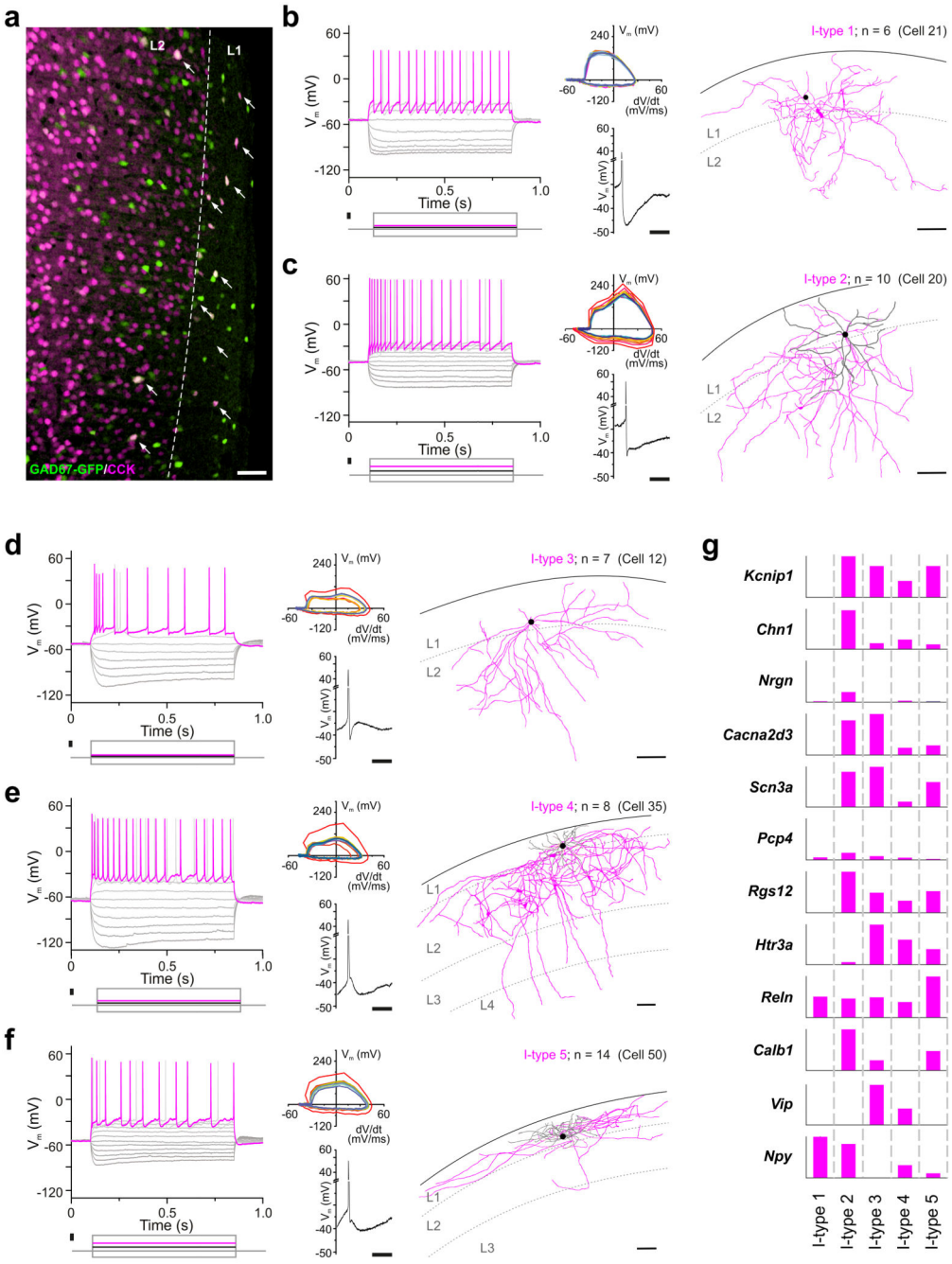

Figure 1. Neurophysiological diversity, distribution and representative molecular marks of CCK interneurons

(a) Confocal photomicrograph of DsRed/GFP dual-labeled neurons (*arrows*) in layer (L)1 of the somatosensory cortex of a $CCK^{BAC/dsRedT3}$:$GAD67^{gfp/+}$ mouse (Supplementary Fig. 1a). *Scale bar* = 50 μm. **(b-f)** Representative current-clamp recordings of dual-tagged CCK^{DsRed}/$GAD67^{gfp}$ interneurons (*"I-type"* 1-5). At the left of each panel, AP responses (*top*) to square current pulses (*bottom*) are shown. Phase-plane plots of the APs rising from 2x rheobase current injection (*top right*) and rheobasic APs (*bottom right*) are depicted for every neuronal subtype. In phase-plane plots, the first AP is red and subsequent APs shift

from warm to cool blue color. For the rheobasic AP, the *y*-axis between −20 mV to +30 mV was omitted to emphasize AHP and ADP characteristics. *Vertical scale bar* = 200 pA, *horizontal scale bar* = 25 ms. To the right of each panel, morphological reconstruction of a representative biocytin-filled interneuron for each subclass is shown. *Scale bar* = 100 μm. Axons are in red, while dendrites are shown in grey. **(g)** Cell-type-specific expression of a voltage gated K^+-channel interacting protein (*Kcnip1*), a GTPase-activating protein (*Chn1*), a protein kinase C substrate (*Nrgn*), a Ca^{2+} channel subunit (*Cacna2d3*), a Na^+ channel subunit (*Scn3a*), Purkinje cell protein 4 (*Pcp4*), a G protein-signaling regulator (*Rgs12*), serotonin receptor subtype 3a (*Htr3a*), reelin (*Reln*), a superficial layer-specific marker, calbindin D28k (*Calb1*), a Ca^{2+}-binding protein, vasoactive intestinal polypeptide (*Vip*) and neuropeptide Y (*Npy*) in sub-classified "*I-type*" CCK^+ interneurons.

Europe PMC Funders Author Manuscripts

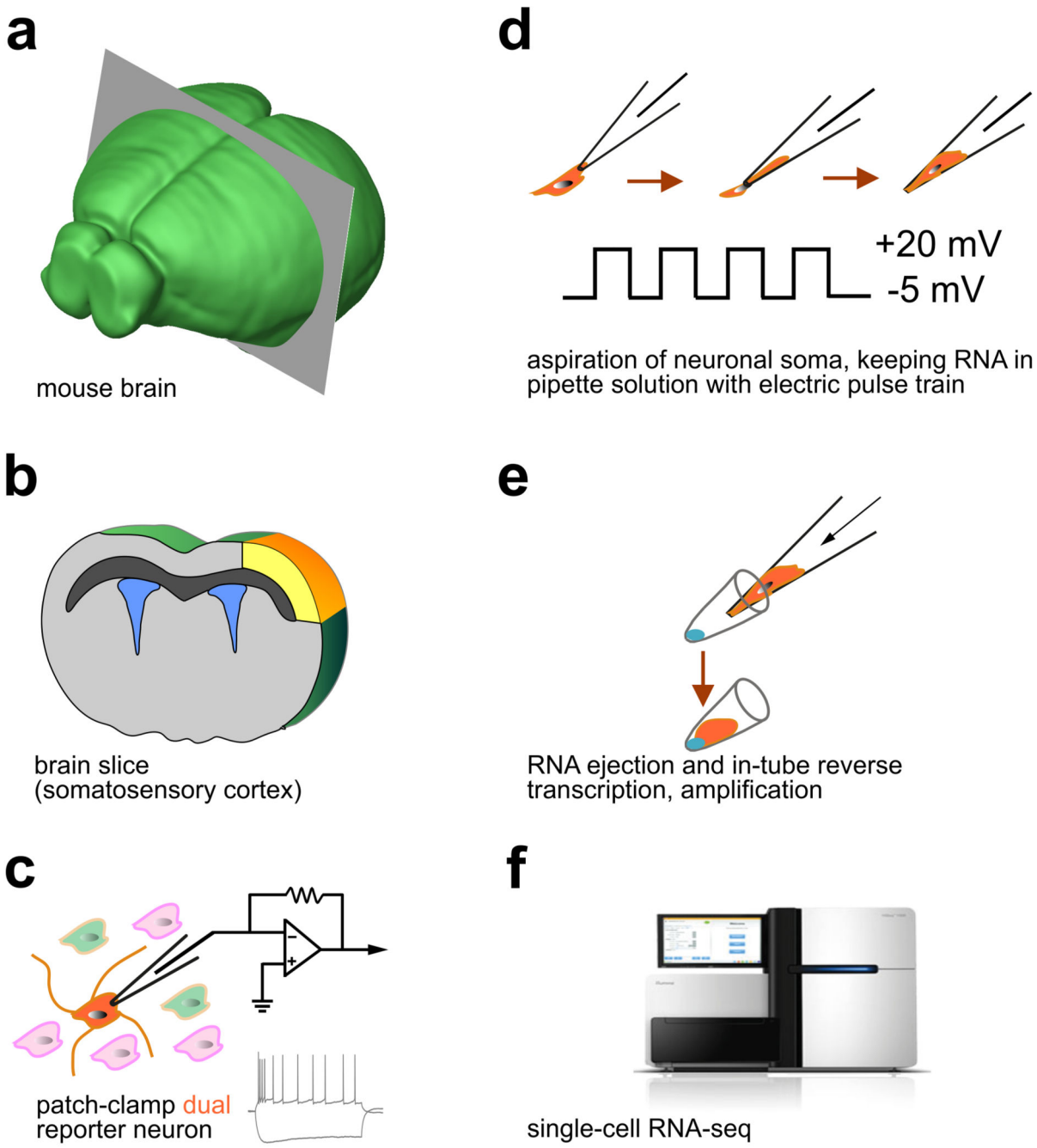

Figure 2. Work-flow diagram of *Patch-seq* procedures

(a) Coronal cutting plane of a mouse brain to access the somatosensory cortex. **(b)** *Ex vivo* brain slice anatomy with the somatosensory cortex highlighted in yellow/orange. **(c)** Whole-cell patch clamp recording of $DsRed^{+}/GFP^{+}$ dual-tagged interneurons. **(d)** Aspiration of neuronal somata was followed by square voltage pulses from −5 mV (holding potential) to +20 mV, whilst maintaining negative pressure. **(e)** The sample was then expelled into lysis buffer, which allows for in-tube reverse transcription by PCR. **(f)** Single-cell RNA sequencing was performed on an Illumina Hiseq2000 instrument.

Europe PMC Funders Author Manuscripts

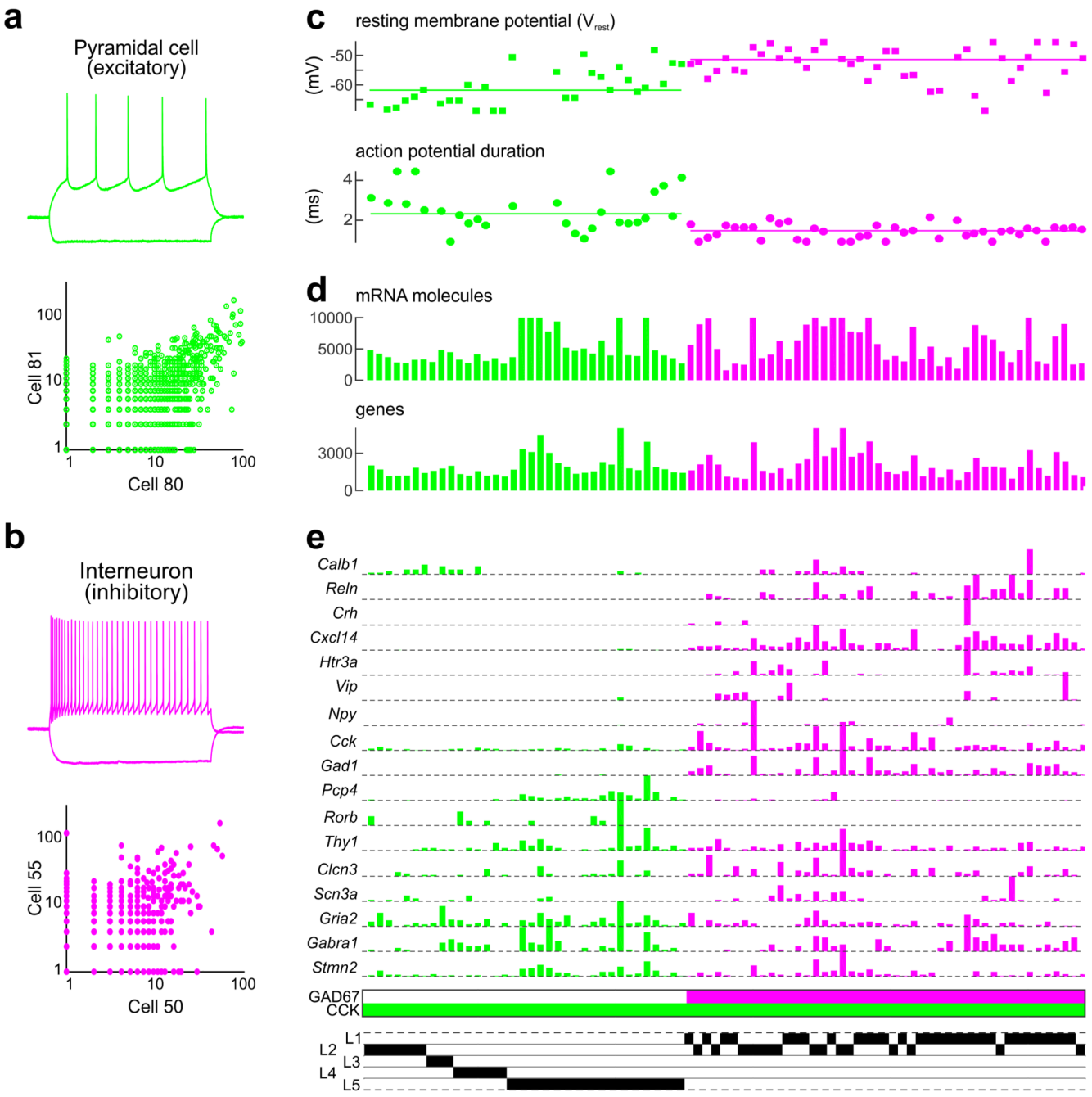

Figure 3. Overview of *Patch-seq* methodology

(a) Analysis of patch-clamp recordings from pyramidal cells and interneurons using large sets of parameters for neuronal classification. Scatter plots between pairs of excitatory and inhibitory neurons reveal high reproducibility. **(b)** Resting membrane potential (V_{rest}, *top*) and AP duration (*bottom*) are shown as examples that, among many others, distinguish (excitatory) pyramidal cells and (inhibitory) interneurons. **(c)** Bar plots showing the total number of mRNA molecules (*top*) and the corresponding number of detected genes (*bottom*) for each cell in the dataset. **(d)** Bar plots showing mRNA molecule counts per cell for select

genes at specified anatomical positions. **(e)** Differential gene expression and layer (L) positioning by pyramidal cells (*green*) and interneurons (*magenta*). *Thy1, Stmn2* are pan-neuronal markers, *Gad1* is a paninterneuron marker and *Calb1, Pcp4* are markers for pyramidal cells in superficial and deep cortical layers[11], respectively.

Europe PMC Funders Author Manuscripts

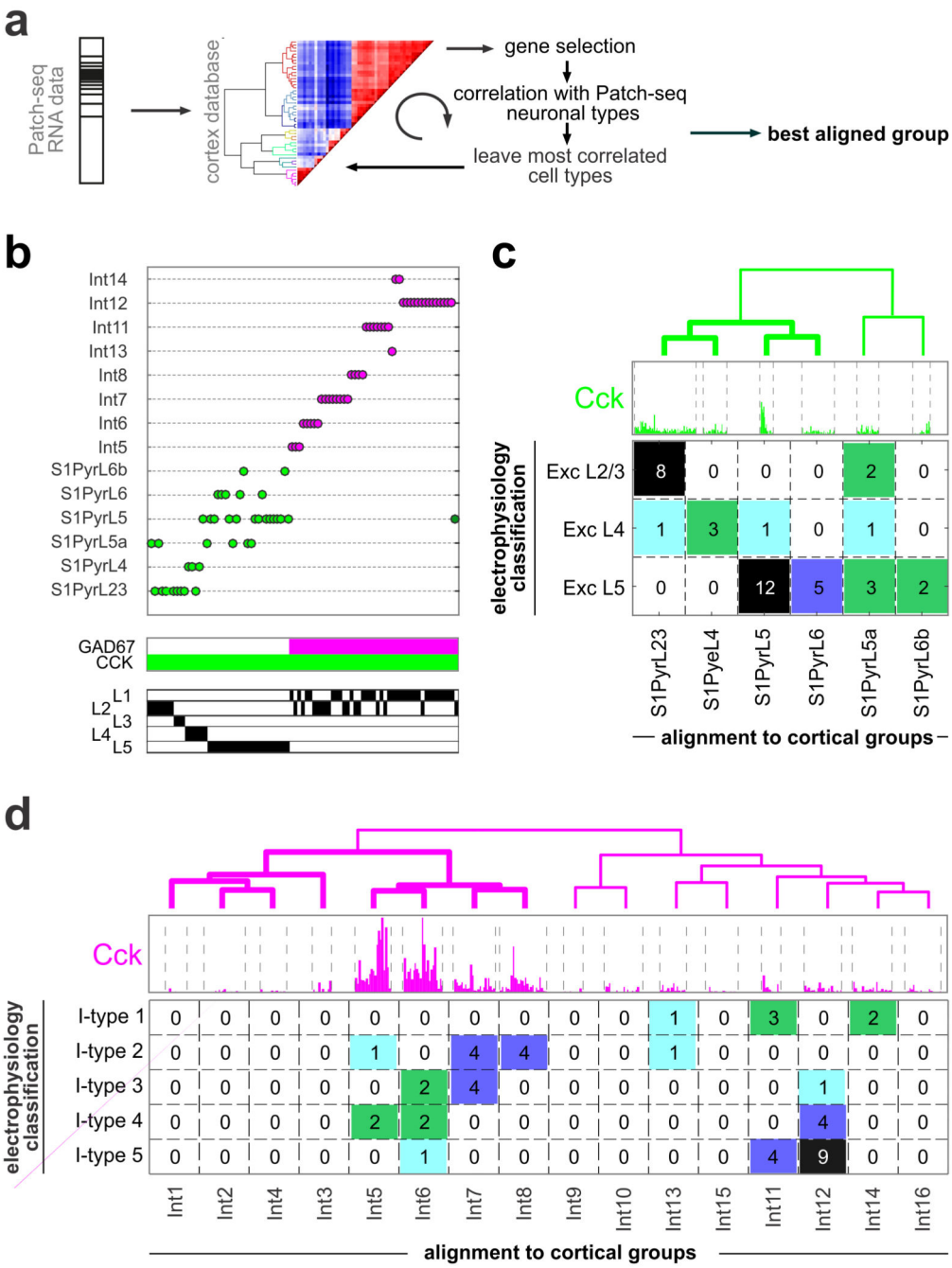

Figure 4. Molecular classification and validation of *Patch-seq*-sampled neurons using a large cortical dataset

(a) Schema of the correlation-based classification process used to align identified neurons in Fig. 1b to previously described pyramidal cell (Supplementary Fig. 1b) and interneuron subtypes. **(b)** Classification results for each cell in our dataset after fitting the best alignment. **(c,d)** Compliance of the electrophysiology-based classification with molecular clustering of pyramidal cells **(c)** and interneurons **(d)**. Dendrograms depict cluster distances

Europe PMC Funders Author Manuscripts

between neuronal subtypes (*top*). Bar plots denote *Cck* mRNA copy numbers in respective cell types (*below*).

Europe PMC Funders Author Manuscripts

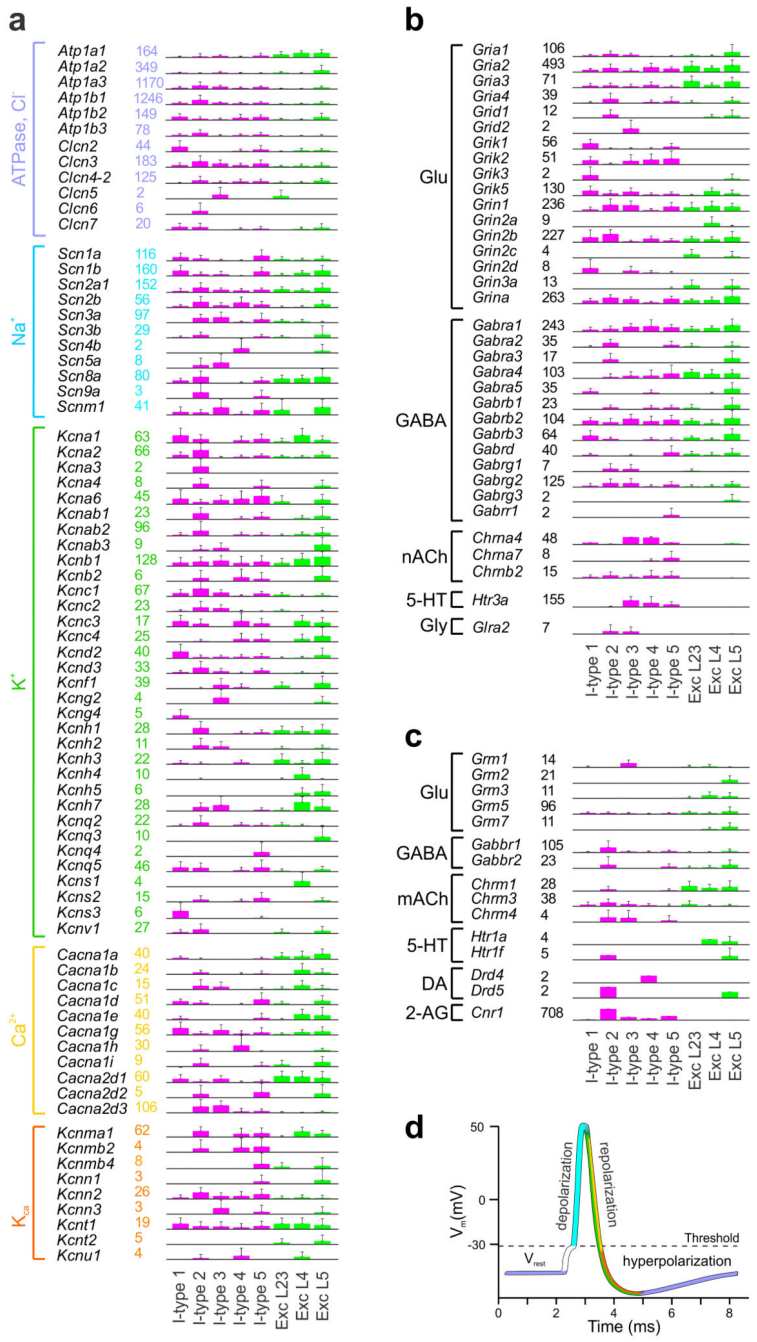

Figure 5. Cell-type specific quantitative expression of ion channel and receptor genes in CCK$^+$ interneurons and pyramidal cells

(a) Differential expression of Na^+/K^+-ATPase, voltage-gated Cl^-, Na^+, K^+, Ca^{2+} and Ca^{2+}-activated K^+ (K_{Ca}) ion channel subunits. **(b)** Ligand-gated ionotropic channel subunits of glutamatergic (Glu), GABAergic (GABA), nicotinic acetylcholinergic (nACh), serotonergic (5-HT) and glycinergic (Gly) receptors. **(c)** Subunits of Glu, GABA, muscarinic acetylcholine (mACh), dopamine (DA) and 2-arachidonoylglycerol (2-AG)-activated metabotropic receptors. Numbers correspond to mRNA molecule counts. Error bars reveal

s.d. Interneuron and pyramidal cell subtypes were color coded in red and green, respectively. **(d)** Schema of an AP indicating its specific phases: rest (V_{rest})/subthreshold (magenta), depolarization (cyan), repolarization (green/yellow) and hyperpolarization (green/orange). Color-codes accord with those of the voltage-gated ion channels determining fast changes in membrane voltage.

Europe PMC Funders Author Manuscripts

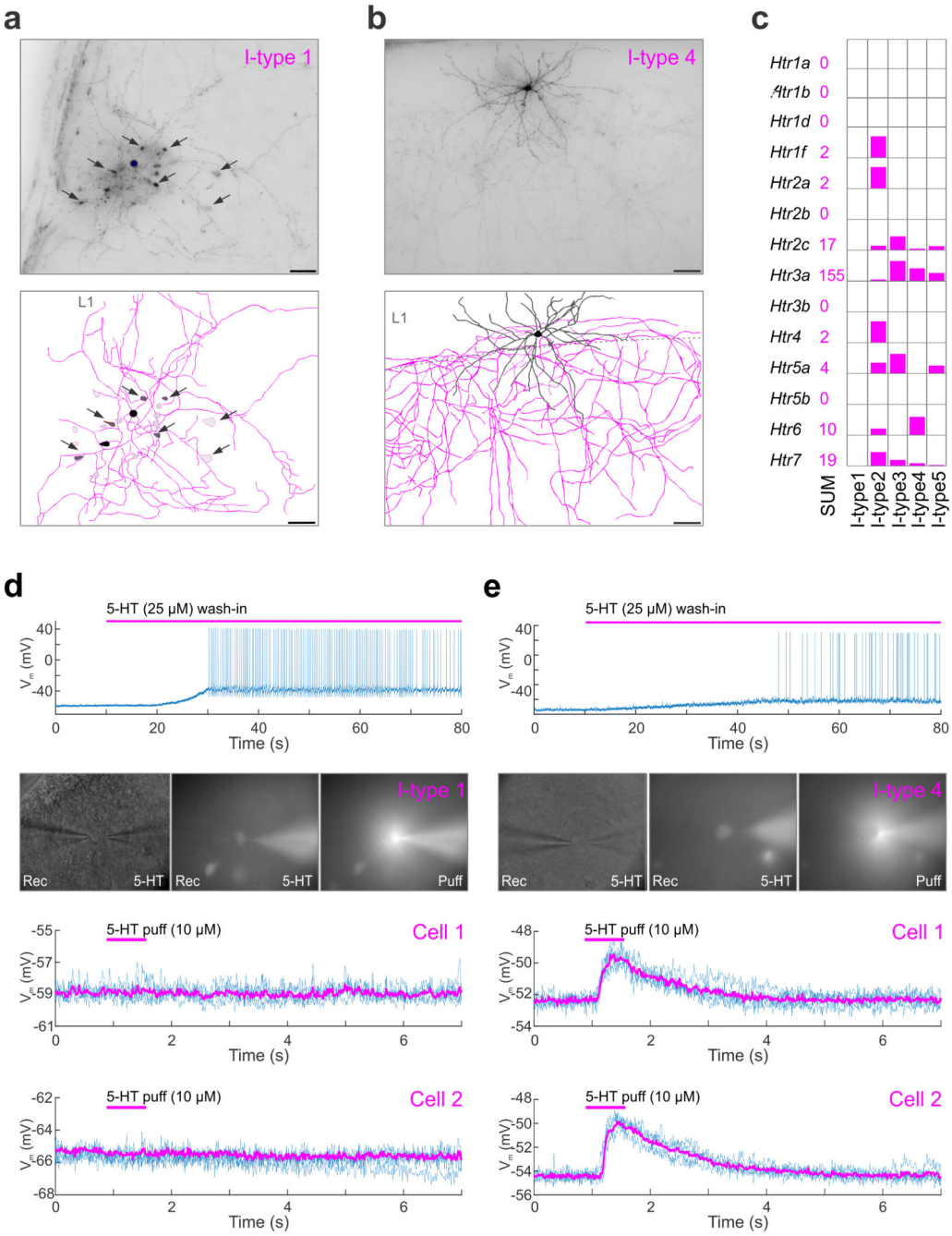

Figure 6. Compliance of RNA-seq predictions with the neurophysiological phenotype of cortical interneurons

(a) Orthogonal image stack of 3,3′-diamonobenzidine (DAB)-stained *I-type 1* interneuron (*top*) and reconstruction of its processes, including dye-coupled neighbors (*bottom*). **(b)** *I-type 4* interneuron processed as above (*top*) and its reconstruction (*bottom*). *Scale bars* = 100 µm. **(c)** Subclass-specific quantitative assessment of mRNA expression for ionotropic and metabotropic 5-HT receptor subunits in interneurons. **(d,e)** *Top*: Representative AP firing by *I-type 1* **(d)** and *I-type 4* **(e)** interneurons upon bath-applied 5-HT (25 µM). *Middle*:

Differential interference and epifluorescence microscopy images (60x) of the recorded cells, suggesting identical 5-HT (10 μM) load upon focal microejection ("puff"). *Bottom*: Membrane potential responses to focal 5-HT application. Two examples (Cell 1,2) per group are shown.

Europe PMC Funders Author Manuscripts